Spatial resolution of 3-D downward extrapolation of incomplete data

C.P.A. Wapenaar, Delft University of Technology, and W.E.A. Rietveld, Delft University of Technology, presently at Amoco

Summary

Three-dimensional prestack downward extrapolation of a complete areal survey over a point diffractor yields a circular symmetric resolution function with the main lobe width being approximately $6\lambda/5$. In practice, however, the sampling distance of the sources and detectors never fulfils the anti-aliasing condition in the x- as well as in the y-direction. In this paper we analyze an extreme case of spatial undersampling, i.e., we consider a single line of sources along the x-axis and a single line of detectors along the y-axis. For this situation the "matched filter approach" cannot be used. We propose a "true amplitude" operator that is adapted for this acquisition configuration. Although its resolution function is no longer circular symmetric and side lobes occur, its main lobe is only approximately $\sqrt{2}$ times wider than in the case of full areal acquisition. Hence, even for this extreme case of spatial undersampling, reasonable images can be obtained. This is illustrated with a prestack migration example of physical model data.

Introduction

Three-dimensional downward wave field extrapolation can be carried out very accurately when the wave fields are sampled on a regular two-dimensional grid along the surface and when the gridsize is equal to or less than half the smallest wavelength (anti-aliasing condition). In seismic practice, however, the grids are often not regular. Moreover, the sampling distance of the sources and detectors never fulfils the anti-aliasing condition in the x- as well as in the y-direction. In *poststack* applications these problems are 'solved' by sorting the midpoints between sources and detectors into a regular grid of 'bins'.
This paper aims at analyzing the effects of spatial undersampling of 3-D data on *prestack* wave equation based processing. In particular the spatial resolution of 3-D downward extrapolation of incomplete data will be analyzed analytically and a true amplitude operator will be proposed. Moreover, prestack migration results will be presented of an "incomplete data acquisition experiment" that has been conducted in our physical modeling facility.

Forward model of 3-D reflection data

Consider the linearized one-way representation for primary reflection data (i.e., after decomposition into downgoing and upgoing waves and after surface related multiple elimination):

$$P^-(\mathbf{x}_D,\mathbf{x}_S) = \int_\Omega W^-(\mathbf{x}_D,\mathbf{x})\hat{R}^+(\mathbf{x})W^+(\mathbf{x},\mathbf{x}_S)S^+(\mathbf{x}_S)d^3\mathbf{x}, \quad (1)$$

with $\mathbf{x} = (x, y, z)$. The frequency ω is omitted for notational convenience. S^+ is a one-way source for downgoing waves, W^+, $\hat{R}^+$ and W^- describe downward propagation from $\mathbf{x}_S$ to $\mathbf{x}$, reflection at $\mathbf{x}$ and upward propagation from $\mathbf{x}$ to $\mathbf{x}_D$, respectively. Finally, P^- is the received upgoing wave field at $\mathbf{x}_D$.
In the following we consider for convenience a source function with unit amplitude, i.e. $S^+ = 1$. Moreover, we consider a single point diffractor with unit amplitude at $\mathbf{x} = \mathbf{x}_R$, according to $\hat{R}^+(\mathbf{x}) = \delta(\mathbf{x} - \mathbf{x}_R)$. Hence, equation (1) simplifies to

$$P^-(\mathbf{x}_D, \mathbf{x}_S) = W^-(\mathbf{x}_D, \mathbf{x}_R) W^+(\mathbf{x}_R, \mathbf{x}_S). \quad (2)$$

For a homogeneous macro model the propagators W^+ and W^- are shift invariant: $W^+(\mathbf{x}_R, \mathbf{x}_S) = W^+(\mathbf{x}_R - \mathbf{x}_S, \mathbf{0})$ and $W^-(\mathbf{x}_D, \mathbf{x}_R) = W^-(\mathbf{x}_D - \mathbf{x}_R, \mathbf{0})$. Replacing $W^+(\mathbf{x}, \mathbf{0})$ and $W^-(\mathbf{x}, \mathbf{0})$ by one and the same propagator $W(\mathbf{x})$ and slightly modifying the notation yields

$$P^-(x_D, y_D, 0|x_S, y_S, 0) = \quad (3)$$
$$W(x_D - x_R, y_D - y_R, z_R) W(x_R - x_S, y_R - y_S, z_R),$$

where

$$W(x, y, z) = \frac{1}{2\pi} \frac{1 + jkr_3}{r_3} \frac{z}{r_3} \frac{\mathrm{e}^{-jkr_3}}{r_3}, \quad (4)$$

with the '3-D distance' r_3 defined as $r_3 = \sqrt{x^2 + y^2 + z^2}$ and $k = \omega/c$, ω being the angular frequency and c the propagation velocity. Note that the source at $(x_S, y_S, 0)$ as well as the diffractor at (x_R, y_R, z_R) are assumed to behave as dipoles.

True amplitude three-dimensional downward extrapolation of full 3-D data

In this section we analyze 3-D downward extrapolation of the data, described in the previous section. We assume that the sampling distance of the sources and detectors fulfils the anti-aliasing conditions in the x- as well as in the y-direction. Hence, for this analysis we may as well use a continuous formulation. The only approximation in this section will be due to the matched filter, which suppresses the evanescent part of the wave field.
The expression for full 3-D downward extrapolation of sources and detectors to an arbitrary depth level z reads

$$P^-(\xi_D, \eta_D, z|\xi_S, \eta_S, z) = \overbrace{\underbrace{\int\int\int\int}_{-\infty}}^{\infty} F(\xi_D - x_D, \eta_D - y_D, z) \times$$
$$P^-(x_D, y_D, 0|x_S, y_S, 0) F(x_S - \xi_S, y_S - \eta_S, z) dx_D dy_D dx_S dy_S, \quad (5)$$

where $F(x, y, z)$ represents the matched filter for a homogeneous macro model, given by $F(x, y, z) = W^*(x, y, z)$, where * denotes complex conjugation and where $W(x, y, z)$ is defined in equation (4). In the following we consider only the zero-offset result, according to $P^-_{ZO}(\xi, \eta, z) = P^-(\xi, \eta, z|\xi, \eta, z)$. Substitution of the forward model, defined in equation (3), gives

$$P^-_{ZO}(\xi, \eta, z) = P_D(\xi, \eta, z) P_S(\xi, \eta, z), \quad (6)$$

where

$$P_D(\xi, \eta, z) = \quad (7)$$
$$\int_{-\infty}^{\infty} \int_{-\infty}^{\infty} F(\xi - x_D, \eta - y_D, z) W(x_D - x_R, y_D - y_R, z_R) dx_D dy_D$$

and

$$P_S(\xi, \eta, z) = P_D(\xi, \eta, z). \quad (8)$$

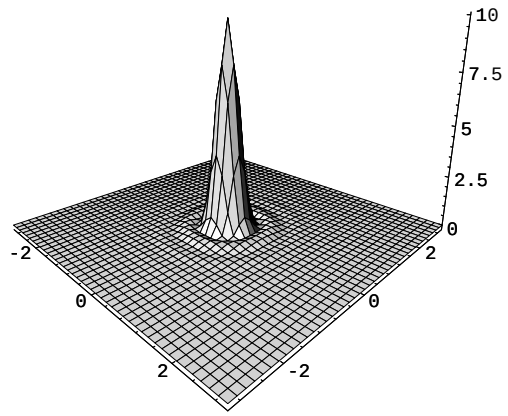

Figure 1: Spatial resolution of 3-D downward extrapolation of full 3-D data. The horizontal axes have been normalized with respect to the wavelength.

Using some basic results of Fourier theory, we may express $P_D(\xi,\eta,z)$ in terms of the Fourier transforms of W and F, according to

$$P_D(\xi,\eta,z) = \frac{1}{4\pi^2}\int_{-\infty}^{\infty}\int_{-\infty}^{\infty}\tilde{F}(k_x,k_y,z)\ \times \tag{9}$$
$$\tilde{W}(k_x,k_y,z_R)\mathrm{e}^{-j\{k_x(\xi-x_R)+k_y(\eta-y_R)\}}dk_xdk_y,$$

where $\tilde{W}$ and $\tilde{F}$ are the spatial Fourier transforms of W and F, respectively, according to

$$\tilde{W}(k_x,k_y,z_R) = \mathrm{e}^{-jk_zz_R} \quad \text{and} \quad \tilde{F}(k_x,k_y,z) = \mathrm{e}^{+jk_z^*z}, \tag{10}$$

where the vertical wavenumber k_z is defined for *propagating* waves (i.e., for $k_x^2+k_y^2 \le k^2$) according to $k_z = +\sqrt{k^2-k_x^2-k_y^2}$ with $k_z^* = k_z$ and for *evanescent* waves (i.e., for $k_x^2+k_y^2 > k^2$) according to $k_z = -j\sqrt{k_x^2+k_y^2-k^2}$ with $k_z^* = -k_z$. Note that $\tilde{F}$ is the exact inverse of $\tilde{W}$ for propagating waves, whereas it suppresses evanescent waves. Substituting these expressions into equation (9) yields

$$P_D(\xi,\eta,z) = \frac{1}{4\pi^2}\underbrace{\int\int}_{\substack{\text{prop.}\\ \text{waves}}}\mathrm{e}^{-jk_z(z_R-z)}\mathrm{e}^{-j\{k_x(\xi-x_R)+k_y(\eta-y_R)\}}dk_xdk_y \tag{11}$$
$$+\frac{1}{4\pi^2}\underbrace{\int\int}_{\text{evan. waves}}\mathrm{e}^{-jk_z(z_R+z)}\mathrm{e}^{-j\{k_x(\xi-x_R)+k_y(\eta-y_R)\}}dk_xdk_y.$$

Next we evaluate $P_D(\xi,\eta,z)$ for the diffractor depth $z=z_R$, ignoring the erroneous contribution of the evanescent waves. This is done most conveniently if we introduce polar coordinates, according to $\xi-x_R = r\cos\phi$, $\eta-y_R = r\sin\phi$, $k_x = k_r\cos\theta$, $k_y = k_r\sin\theta$ and $dk_xdk_y = k_rd\theta dk_r$. Hence, for the first integral in equation (11) we now obtain

$$P_D(\xi,\eta,z_R) = \frac{1}{4\pi^2}\int_0^k\Big(\int_0^{2\pi}\mathrm{e}^{-jk_rr\cos(\theta-\phi)}d\theta\Big)k_rdk_r \tag{12}$$
$$= \frac{1}{2\pi}\int_0^k \mathrm{J}_0(k_rr)k_rdk_r = \frac{k}{2\pi}\frac{\mathrm{J}_1(kr)}{r},$$

where $r=\sqrt{(\xi-x_R)^2+(\eta-y_R)^2}$ and where J_n is the n'th order Bessel function. Using equation (6) we finally find

$$P_{ZO}^{-}(\xi,\eta,z_R) = P_D(\xi,\eta,z_R)P_S(\xi,\eta,z_R) = \frac{k^2}{4\pi^2}\frac{\mathrm{J}_1^2(kr)}{r^2}, \tag{13}$$

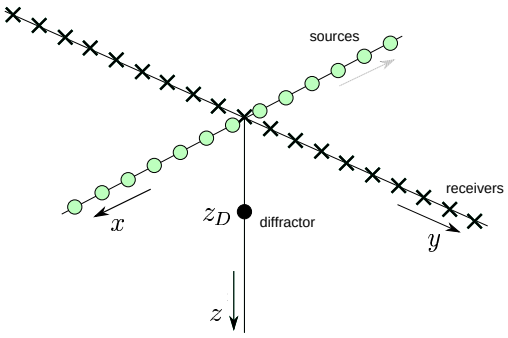

Figure 2: Incomplete data acquisition configuration. The situation is shown for $x_R = y_R = 0$.

see Figure 1 for $x_R = y_R = 0$. This result represents the (monochromatic) zero-offset response of the diffractor, 'measured' at the depth level of the diffractor. Instead of a spatial delta function we observe a circular symmetric resolution function. The limited resolution is due to the suppression of the evanescent wave field. The width of the main lobe (measured at the first zero crossing) is approximately $6\lambda/5$, where the wavelength λ is defined as $\lambda = 2\pi/k$. Note that the side lobes have very low amplitudes.

True amplitude three-dimensional downward extrapolation of incomplete data

As was mentioned in the introduction, in seismic practice the sampling distance of the sources and detectors never fulfils the anti-aliasing condition in the x- as well as in the y-direction. In this section we analyze an extreme situation of spatial undersampling and we derive a true amplitude propagator. We consider a situation with sources only along the x-axis and detectors only along the y-axis, see Figure 2. Hence, the sources are severely undersampled in the y-direction, but we assume that they are properly sampled in the x-direction. Similarly, the detectors are severely undersampled in the x-direction, but we assume that they are properly sampled in the y-direction. Hence, for our analysis we may use again a continuous formulation, if we make the following replacement

$$P^-(x_D, y_D, 0|x_S, y_S, 0) \rightarrow \delta(x_D) P^-(x_D, y_D, 0|x_S, y_S, 0)\delta(y_S). \tag{14}$$

Substituting this into equation (5) for 3-D downward extrapolation and selecting the zero-offset result yields

$$P^-_{ZO}(\xi, \eta, z) = \int_{-\infty}^{\infty}\int_{-\infty}^{\infty} F(\xi, \eta - y_D, z) \;\times \tag{15}$$
$$P^-(0, y_D, 0|x_S, 0, 0) F(x_S - \xi, -\eta, z) dy_D dx_S.$$

Taking for P^- again the response of a point diffractor at (x_R, y_R, z_R) in a homogeneous macro model (equation 3, with $x_D = 0$ and $y_S = 0$) yields

$$P^-_{ZO}(\xi, \eta, z) = P_D(\xi, \eta, z) P_S(\xi, \eta, z), \tag{16}$$

where

$$P_D(\xi, \eta, z) = \int_{-\infty}^{\infty} F(\xi, \eta - y_D, z) W(-x_R, y_D - y_R, z_R) dy_D \tag{17}$$

and

$$P_S(\xi, \eta, z) = \int_{-\infty}^{\infty} W(x_R - x_S, y_R, z_R) F(x_S - \xi, -\eta, z) dx_S. \tag{18}$$

Note that this time P_D and P_S are different. Since in equations (17) and (18) we consider one-dimensional integrals, it is useful to replace the expressions for W and F by pseudo 2-D propagators, according to

$$\begin{aligned} F(\xi, \eta - y_D, z) &\rightarrow F(\eta - y_D, z^{(\xi)}); \quad z^{(\xi)} = \sqrt{z^2 + \xi^2}, \\ W(-x_R, y_D - y_R, z_R) &\rightarrow W(y_D - y_R, z_R^{(x)}); \quad z_R^{(x)} = \sqrt{z_R^2 + x_R^2}, \\ W(x_R - x_S, y_R, z_R) &\rightarrow W(x_R - x_S, z_R^{(y)}); \quad z_R^{(y)} = \sqrt{z_R^2 + y_R^2}, \\ F(x_S - \xi, -\eta, z) &\rightarrow F(x_S - \xi, z^{(\eta)}); \quad z^{(\eta)} = \sqrt{z^2 + \eta^2}. \end{aligned}$$

Note that $z^{(\xi)}$, $z_R^{(x)}$, $z_R^{(y)}$ and $z^{(\eta)}$ represent 'effective depths'. With these replacements we obtain

$$P_D(\xi, \eta, z) = \int_{-\infty}^{\infty} F(\eta - y_D, z^{(\xi)}) W(y_D - y_R, z_R^{(x)}) dy_D \qquad (19)$$

and

$$P_S(\xi, \eta, z) = \int_{-\infty}^{\infty} W(x_R - x_S, z_R^{(y)}) F(x_S - \xi, z^{(\eta)}) dx_S, \qquad (20)$$

where

$$W(h, z) = \frac{1}{2\pi} \frac{1 + jkr_2}{r_2} \frac{z}{r_2} \frac{\mathrm{e}^{-jkr_2}}{r_2}, \qquad (21)$$

with the '2-D distance' r_2 defined as $r_2 = \sqrt{h^2 + z^2}$, $h = x$ or $h = y$. Note that equations (19) and (20) are fully equivalent with equations (17) and (18). Again we analyze these expressions by introducing the Fourier transforms of propagators W and F. Since we consider incomplete data we cannot use the matched filter approach for F. Instead, in the Fourier domain we define $\tilde{F}$ as $\tilde{W}^{-1}$. Using the method of stationary phase we obtain

$$\tilde{W}(k_h, z) \approx \sqrt{\frac{jk_z}{2\pi z}} \mathrm{e}^{-jk_z z} \rightarrow \tilde{F}(k_h, z) \approx \sqrt{\frac{2\pi z}{jk_z}} \mathrm{e}^{+jk_z z}, \qquad (22)$$

where, for propagating waves (i.e., for $k_h^2 \leq k^2$) we have $k_z = +\sqrt{k^2 - k_h^2}$ and for evanescent waves (i.e., for $k_h^2 > k^2$) we have $k_z = -j\sqrt{k_h^2 - k^2}$. Using the method of stationary phase again yields

$$F(h, z) \approx -jz \frac{\mathrm{e}^{+jkr_2}}{r_2} \quad \text{or} \quad F(h, z) \approx \frac{2\pi r_2}{k} W^*(h, z), \qquad (23)$$

for $h = x$ or $h = y$. Hence, for P_D, as defined in (19), we obtain

$$P_D(\xi, \eta, z) = \frac{1}{2\pi} \int_{-\infty}^{\infty} \tilde{F}(k_y, z^{(\xi)}) \tilde{W}(k_y, z_R^{(x)}) \mathrm{e}^{-jk_y(\eta - y_R)} dk_y, \quad (24)$$

or, ignoring evanescent waves,

$$P_D(\xi, \eta, z) = \frac{1}{2\pi} \int_{-k}^{k} \sqrt{\frac{z^{(\xi)}}{z_R^{(x)}}} \mathrm{e}^{-jk_z(z_R^{(x)} - z^{(\xi)})} \mathrm{e}^{-jk_y(\eta - y_R)} dk_y. \quad (25)$$

We evaluate this expression for the depth of the diffractor $z = z_R$, assuming small ξ / z_R and small x_R / z_R. Hence, $z^{(\xi)} \rightarrow z_R^{(\xi)} = \sqrt{z_R^2 + \xi^2} \approx z_R + \xi^2 / 2z_R$. Similarly, $z_R^{(x)} \approx z_R + x_R^2 / 2z_R$. The terms that are *quadratic* in ξ and x_R will be ignored in the evaluation of equation (25), which contains other terms that are *linear* in η and y_R. Hence, we approximate equation (25) by

$$P_D(\xi, \eta, z_R) \approx \frac{1}{2\pi} \int_{-k}^{k} \mathrm{e}^{-jk_y(\eta - y_R)} dk_y = \frac{\sin(k(\eta - y_R))}{\pi(\eta - y_R)}. \quad (26)$$

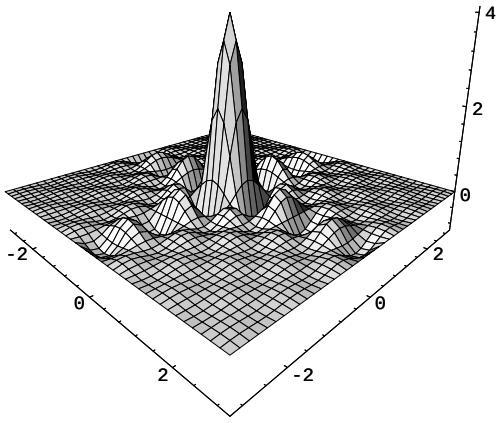

Figure 3: Spatial resolution of 3-D downward extrapolation of incomplete data. The horizontal axes have been normalized with respect to the wavelength.

Similarly, for small η/z_R and small y_R/z_R we obtain

$$P_S(\xi,\eta,z_R) \approx \frac{1}{2\pi}\int_{-k}^{k} \mathrm{e}^{-jk_x(\xi-x_R)}dk_x = \frac{\sin(k(\xi-x_R))}{\pi(\xi-x_R)}. \qquad (27)$$

Using equation (16) we finally find

$$\begin{aligned} P_{ZO}^{-}(\xi,\eta,z_R) &= P_D(\xi,\eta,z_R)P_S(\xi,\eta,z_R) \qquad (28)\\ &\approx \frac{\sin(k(\xi-x_R))}{\pi(\xi-x_R)}\frac{\sin(k(\eta-y_R))}{\pi(\eta-y_R)}, \end{aligned}$$

see Figure 3 for $x_R = y_R = 0$. This result represents the (monochromatic) zero-offset response of the diffractor, 'measured' at the depth level of the diffractor. It is of course not circular symmetric, as was the case with full 3-D data (see Figure 1). The width of the main lobe measured along a diagonal in Figure 3 is $\sqrt{2}$ times the width of the main lobe in Figure 1. Also the side lobes in Figure 3 are more severe. However, looking at the severe undersampling (Figure 2) we may conclude that the resolution is quite acceptable.
Finally we analyze the downward extrapolation result for the situation of an infinite horizontal perfect reflector at depth z_R. This reflector may be seen as a continuous distribution of point diffractors at depth level z_R, hence, the downward extrapolation result is simply obtained by integrating equation (28) along x_R and y_R, according to

$$\int_{-\infty}^{\infty}\int_{-\infty}^{\infty} \frac{\sin(k(\xi-x_R))}{\pi(\xi-x_R)}\frac{\sin(k(\eta-y_R))}{\pi(\eta-y_R)}dx_R dy_R = 1. \qquad (29)$$

This result confirms that F, as defined in equation (23), is indeed a true amplitude inverse propagator.

Numerical examples

The analytical results in the previous sections are approximations for small ξ/z_R, η/z_R, x_R/z_R and y_R/z_R. In this section we check the previously obtained results by a numerical evaluation of equations (25) and we consider some examples where the above mentioned conditions are violated. Figure 4 shows the spatial resolution result for downward extrapolation of incomplete data for a diffractor depth $z_R = 20\lambda$. Note that this numerical result resembles the approximated analytical result very well. Figure 5 is obtained in the same way, but this time for a diffractor depth

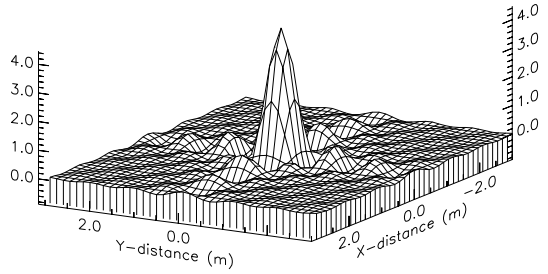

Figure 4: Spatial resolution of numerical 3-D downward extrapolation of incomplete data. The horizontal axes have been normalized with respect to the wavelength. The extrapolation depth equals 20 wavelengths.

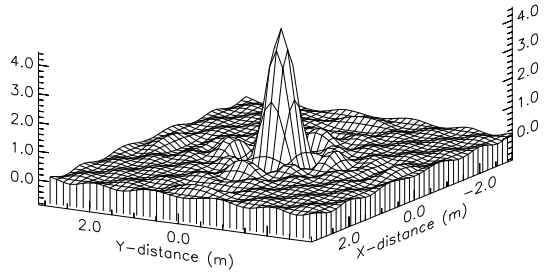

Figure 5: As in Figure 4. The extrapolation depth equals 5 wavelengths.

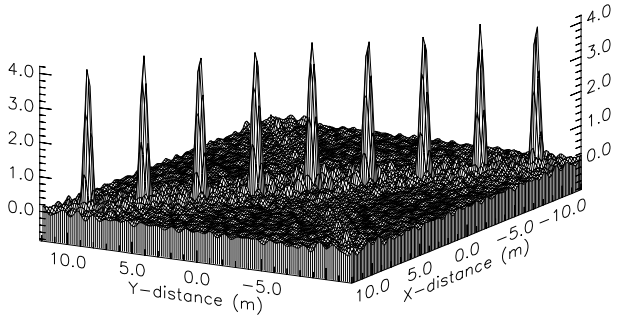

Figure 6: As in Figure 4. Nine diffractor model.

$z_R = 5\lambda$, so that the conditions of small ξ/z_R and η/z_R are violated. In spite of this violation, the character of the resolution function hardly changed. Finally, Figure 6 shows the result for a range of diffractors at $z_R = 20\lambda$, for which the conditions of small x_R/z_R and y_R/z_R are violated. Note again that the resolution function is not seriously distorted.

Physical modeling example

We conducted a physical modeling experiment with the acquisition configuration of Figure 2 over the physical scale model, shown in Figure 7. The scaling factor that has been used is 20,000; distances and times are given at the seismic scale. We modeled 101 shots with 101 receivers each. The frequency range is $20 < f < 70$ Hz. The shot sampling as well as the receiver sampling is 15 m. Because in the modeling facility it is not possible to have intersecting source and receiver lines, we had to make use of reciprocity and the missing near offsets had to be interpolated. Figures 8 and 9 show the 51rst shot record before and after interpolation of the missing near offsets.

The data have been downward extrapolated, using equation (15), with a stepsize $\Delta z = 5$m. Imaging has been performed by integrating the results along the frequency axis.

Figure 10 is a plan view of the model at depth level $z = 400$m. The best imaging results may be expected around the vertical axis

through the intersection of the source and receiver lines. Figure 11 shows a migrated horizontal depth slice at $z = 400$m. Apart from the image of the horizontal reflector, the contours of the dome and the fault can also (just) be recognized (compare with Figure 10). Figures 12 and 13 show migrated vertical cross-sections at $x_D = 3200$m and $y_S = 4400$m, respectively. Note that, particularly in Figure 12, the fault is accurately imaged, despite the severe undersampling. Finally, for comparison Figure 14 shows a migrated vertical cross-section parallel to the source line at $x = 3620$m, obtained by the areal shot record migration of the second author.

Conclusions

It has been shown that 3-D prestack downward extrapolation of full 3-D data yields a circular symmetric resolution function with a width of $6\lambda/5$ and very low side lobes (Figure 1). For an extreme situation of spatial undersampling (Figure 2) it has been shown that the resolution function is still quite acceptable (the width along the diagonal increases by a factor of $\sqrt{2}$, the amplitudes of the side lobes along the main axes increase somewhat, see Figure 3). It has been confirmed in equation (29) that the proposed inverse propagator F (equation 23) yields true amplitude results. It should be noted that the configuration of Figure 2 is an extreme example of spatial undersampling. A more realistic land acquisition configuration consists of a number of parallel source lines and a number of parallel receiver lines. For this configuration true amplitude imaging of the zero-offset reflectivity could be accomplished by applying the true amplitude operator, given by equation (23), divided by the product of the number of source- and receiver lines that contribute to the imaging region of interest.
Of course the results derived in this paper strictly apply only to constant velocity media. However, it is expected that the modification of the matched filter, formulated in equation (23), is approximately valid in inhomogeneous media.

Acknowledgements

We would like to thank Mr E.A. Koek for providing us the model data and Dr D.J. Verschuur and Mr L. Faqi for interpolating the missing small offsets.

layer	velocity (m/s)	density (kg/m^3)
1	1487	1000
2	1018	959
3	2190	1035
4	1018	959
5	1510	1070

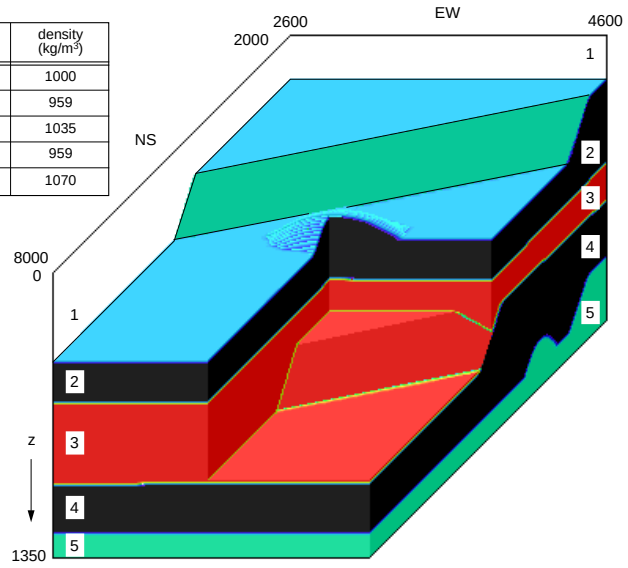

Figure 7: Physical model.

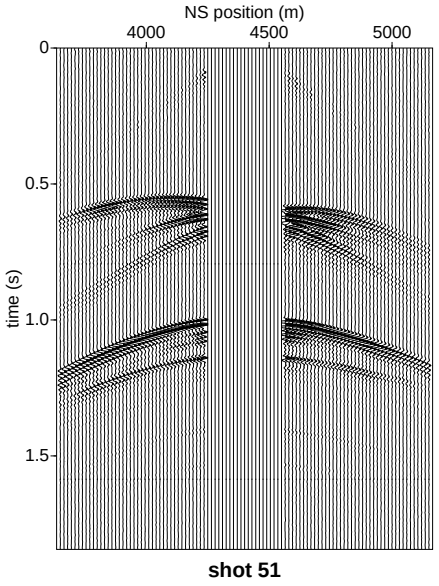

Figure 8: Shot record with missing near offsets.

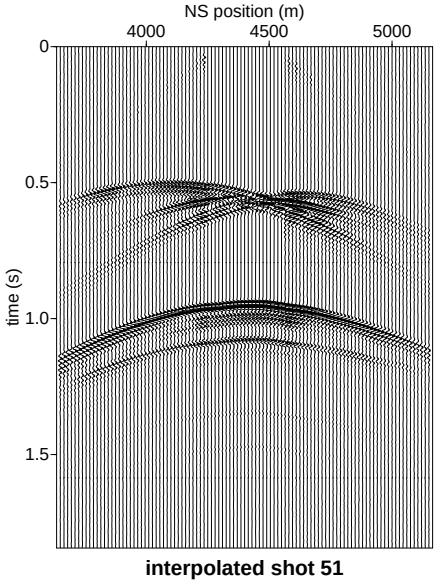

Figure 9: Interpolated shot record.

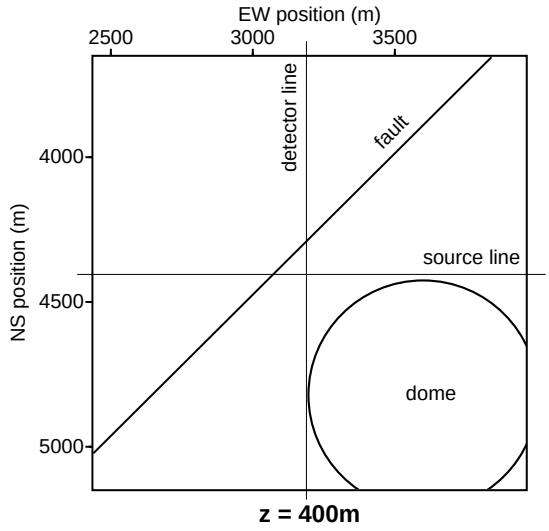

Figure 10: Cross section through model at $z = 400m$.

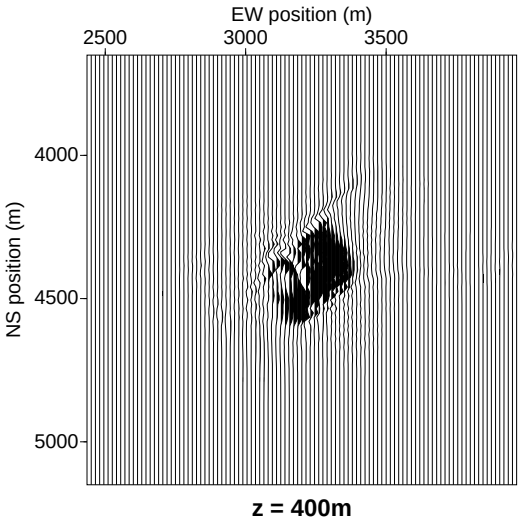

Figure 11: Migrated depth slice at $z = 400m$.

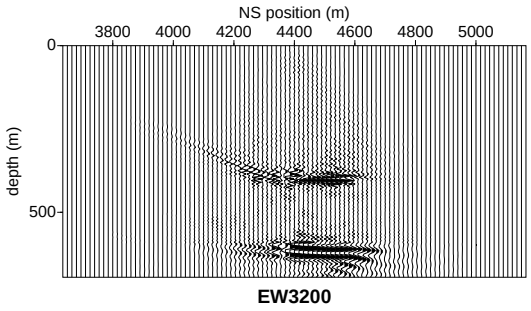

Figure 12: Migrated vertical cross-section along the detector line at $x_D = 3200m$.

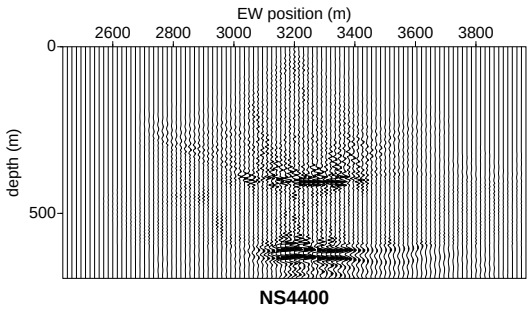

Figure 13: Migrated vertical cross-section along the source line at $y_S = 4400m$.

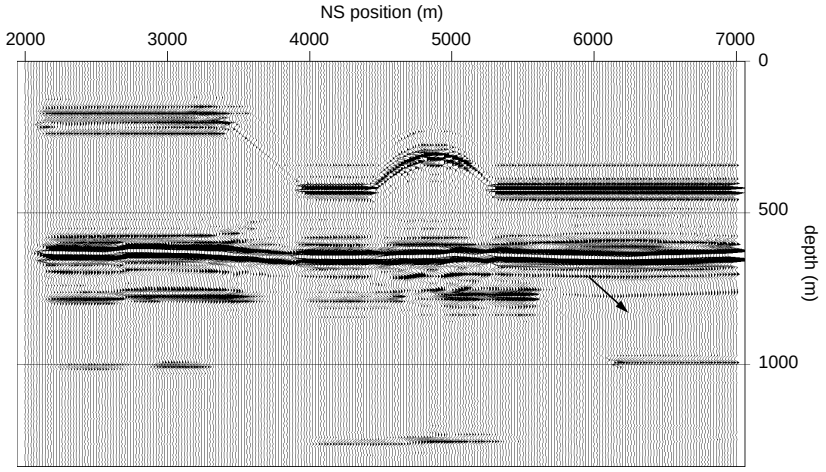

Figure 14: Result of areal shot record migration at $x = 3620\,m$.